Combustion and Flame 160 (2013) 1706–1716

Contents lists available at SciVerse ScienceDirect

Combustion and Flame

journal homepage: www.elsevier.com/locate/combustflame

Direct numerical simulation of lean hydrogen/air auto-ignition in a constant volume enclosure

Rixin Yu *, Xue-Song Bai

Division of Fluid Mechanics, Lund University, Lund, Sweden

ARTICLE INFO

Article history:
Received 24 August 2012
Received in revised form 21 December 2012
Accepted 22 March 2013
Available online 17 April 2013

Keywords:
Direct numerical simulation (DNS)
Three-dimensional
HCCI
Ignition front
Hydrogen combustion

ABSTRACT

This paper reports on two-dimensional (2D) and three-dimensional (3D) direct numerical simulations (DNSs) of the auto-ignition process of a lean H_2/air mixture with temperature stratification in a constant volume enclosure. Detailed chemistry and transport properties are taken into account in the simulations. The combined propagation of spontaneous ignition front and deflagration front is identified and the relation between the reaction front displacement speed and the temperature gradient is verified. The difference between 2D- and 3D-DNS is investigated by comparing the evolutions of global combustion parameters such as the averaged heat release rate, total reaction front area and the averaged displacement speed of the reaction front. The extra spatial dimension in 3D-DNS has been shown to cause a higher velocity strain rate to enhance the heat transfer process, which leads to a delayed but more rapid ignition of the mixture than the 2D-DNS cases. The 3D reaction front surfaces are examined based on the local mean and Gaussian curvatures. By introducing a cutoff Gaussian curvature two types of 3D surface elements, the small sphere fronts and the strong saddle fronts, are defined. The effect of these fronts on the combustion process is studied in terms of their contribution to the total reaction front area, fuel consumption rate and curvature-induced stretch.

1. Introduction

In the past decade homogenous charge compression ignition (HCCI) engines have attracted great attention from the engine industry and the combustion research community owing to its promise of high efficiency and low emission. Contrary to the ideal concept of homogenous ignition, a realistic HCCI combustion occurs in a turbulent environment with certain level inhomogeneity in temperature and sometimes fuel concentration. The reaction front of HCCI combustion is different from the classical flames. Depending on the temperature gradient, the reaction front may propagate as a premixed flame or as an ignition wave [1]. Understanding the fundamental structures of HCCI reaction fronts is important for developing control method of HCCI combustion, e.g. reducing the pressure-rise rate and high noise at high load of engine operation.

Direct numerical simulations (DNSs) have been carried out for generic HCCI processes, e.g. HCCI combustion in a thermally stratified turbulent H_2/air mixture in a two dimensional periodical rectangular domain under constant volume conditions [2–6]. Such simulations are referred to as 2D-DNS. Using this approach, Sankaran et al. [2] studied the effect of the skewness of initial temperature fields on the initial ignition and subsequent heat release of lean fully premixed H_2/air ignition, and they identified the spatial distribution of spontaneous ignition and premixed flame fronts. Chen et al. [3] developed a numerical diagnostics approach for analysis of the DNS results. An indicator of front propagation due to deflagration or spontaneous ignition was proposed based on the local front displacement speed. The diagnostic approach was applied in studies of the effect of the initial temperature and turbulence field on HCCI combustion [4], and the effect of differential diffusion during auto-ignition of a hydrogen/air mixture [5]. 2D-DNS has been used recently to study the effect of more complex fuel (n-heptane with cool flames) in [6] and ignition in mixtures with initial fuel stratification [7].

2D-DNS studies have provided useful insight into the physics of HCCI combustion; however, the physical process takes place in the three dimensional space. The results and conclusions from previous studies may need modifications to account for an extra dimension. In previous studies the diffusion has been shown to play two major roles in affecting HCCI combustion process [3]. The first effect results in the propagation of the deflagration front, the second effect is through dissipation of initial temperature gradient to promote later spontaneous ignition. Since the diffusion is a spatial process, an extra space dimension can fundamentally influence the diffusion process and its roles on the combustion process.

* Corresponding author. Address: Division of Fluid Mechanics, Lund University, S 221 00 Lund, Sweden. Fax: +46 462224717.
E-mail address: Rixin.yu@energy.lth.se (R. Yu).

0010-2180/$ - see front matter © 2013 The Combustion Institute. Published by Elsevier Inc. All rights reserved.
http://dx.doi.org/10.1016/j.combustflame.2013.03.025

Interesting questions regarding the addition of one dimension may arise, such as will the formation and propagation of reaction fronts change and will the dissipation process of temperature gradient be different? If so, how and why? Since the auto-ignition process takes process in turbulent environment, another commonly asked question is regarding the 3D vortex stretching/bending mechanism [8,9] for turbulent energy cascading – will the absence of this mechanism in the previous 2D studies have direct impact on the combustion characteristics? Furthermore, in previous works the reaction fronts are 2D surfaces, the realistic 3D reaction fronts have additional topological structures. With one more curvature than in 2D, the 3D surfaces can be locally saddle/spherical shape. For HCCI combustion it remains unclear how much those 3D surface elements contribute and affect the growth/consumption of reaction fronts.

The 3D-DNS for reacting flow is computationally demanding and requires implementation of accurate and sensitive numerical schemes. For ignition related studies few 3D works [10–12] were performed based on simplified chemistry. With the more expensive detailed-chemistry calculation, even fewer studies were carried out and the applications are limited to either simple setup such as the growth of a premixed flame ball [13,14] or jet, burner typed combustors [15]. A recent review on DNS of combustion applications can be seen in [16]. Furthermore, for ignition related applications, previous comparison of 2D/3D DNS difference was studied only on non-premixed mixture (based on dimensional arguments in [17]), it will be beneficial to study premixed mixture for HCCI combustion.

With the developments in numerical methods and increased availability of large scale computing powers, in this work we present a 3D-DNS of lean hydrogen/air auto-ignition under constant volume HCCI condition that is identical to the one of Chen et al. [3]. To identify the similarity and discrepancy between 3D-DNS results and the results from numerical simulations in low dimensional configurations we performed both 1D and 2D simulations under similar conditions to the 3D case. One goal of this work is to investigate the difference between 2D and 3D DNS for a HCCI combustion application. Factors affecting the ignition process, such as temperature field mixing, heat release, area and propagation speed of reaction front will be investigated. The second goal of the work is to characterize effects due to the uniquely 3D front surfaces. The saddle/spherical surfaces elements and their contributions to the growth/consumption of reaction fronts are examined.

The paper is organized as follow. In Section 2 the computational methods and setups are briefly described. The computational results are discussed in Sections 3, where the solver is first verified by comparing lower dimensional results with previous studies, followed by a qualitative description of 3D reaction fronts. The 2D/3D difference will then be studied in details, followed by the final discussion of front stretch, the 3D reaction front topology and the contribution of three-dimensional curvatures to the reaction front propagation.

2. Numerical methods and simulation conditions

An in-house DNS solver for low Mach number reacting flows is employed taking into account detailed transport properties and detailed chemical kinetics. The turbulent reacting flows are governed by the Navier–Stokes equations and transport equations for species mass fractions and energy. With the low Mach number assumption the stability limit requiring for small time steps due to the high acoustic speed is removed, therefore larger time steps can be used to advance the discretized governing equations to achieve an appreciable computational speedup.

To maintain numerical stability when simulating low speed reacting flow (avoiding spurious heat release [18] in the presence of large density ratio), the solver method is based on using the material-derivative form of continuity equations [19,20] instead of the predictor/corrector approach [21,22]. This procedure leads to a variable coefficient Poisson equation for hydrodynamic pressure which is iteratively solved using the Multigrid method. The temporal integration of a convection–diffusion–reaction (CDR) problem is often performed using an operator splitting technique. We use the 2nd order symmetrical Strang splitting algorithm [23]; the integration of one full time step of the stiff reaction rates is placed in between of two half-step integrations of the diffusion and convection terms. The integration of the diffusion terms is further split into multiple sub-steps of explicit integrations. The sub-steps integration starts with a 2nd order Runge–Kutta step and then continues with the 2nd order Adams–Bashforth steps. The number of sub steps corresponding to each of the three physical diffusion processes (i.e. the species diffusions in the species mass equations, the heat conduction in the energy equation and the viscous forces in the momentum equations) is determined independently by adjusting the sub-step size close to half of the maximum value allowed by the diffusion stability limit of each process. The discretization of all spatial terms is made using a 6th order central difference scheme except for the convective terms in the species mass fraction and energy equations, where a 5th order WENO scheme [24] is used to avoid unphysical numerical oscillations. The spatial/temporal accuracy of the numerical scheme has been verified with grid/time-step dependency tests. The code is written in a vector form enabling simulations from 1D to 3D. Detailed description of the numerical method is given in [25].

The integration of chemical reaction rates involved in detailed chemical kinetic mechanisms is performed using an accurate stiff solver, DVODE [26]. In this study, the H_2/air mechanism of Li et al. [27], involving 9 species and 21 reactions is used. The mechanism is an updated version of that used in the 2D-DNS of Chen et al. [3]. The transport properties, e.g. species diffusion coefficients, thermal conductivity and viscosity, are mixture averaged based on the individual species obtained from a thermodynamic database. To reduce the computational cost, the transport properties are evaluated only at the beginning of each time step and then interpolated to the sub-steps. The accuracy is shown to maintain second order in time while the efficiency of the computation is enhanced substantially [25,28].

The computation case is a 3D extension of the 2D setup used by Chen et al. [3]. The computational domain is a 4.1 mm^3 cube with periodical boundary conditions on all six sides. A uniform 512^3 Cartesian grid is used to discretize the domain. The H_2/air mixture has an equivalence ratio of $\Phi = 0.1$, initial temperature of $T_0 = 1070$ K and initial pressure of $P_0 = 41$ atm. The initial fluctuating turbulence field ($\mathbf{u}(\mathbf{x})$) is numerically generated using a variant of Kraichnan's method [29] modified for using Fast Fourier Transform (FFT) to synthesize waves

$$\mathbf{u}(\mathbf{x}) = \sum_{k_1,k_2,k_3=1-1/2N}^{1/2N} \hat{\mathbf{u}}(\mathbf{k}) \exp\left(\frac{2\pi}{N} i\mathbf{k}\cdot\mathbf{x}\right), \tag{1}$$

where $i^2 = -1$, k is the wave vector and N is grid number in one direction. The complex Fourier mode vector $\hat{\mathbf{u}}$ is given by:

$$\hat{\mathbf{u}}(\mathbf{k}) = \begin{cases} \sqrt{\frac{E(k)}{2\pi k^2}} \frac{\exp(\alpha+i\beta)\times\mathbf{k}}{|\exp(\alpha+i\beta)\times\mathbf{k}|} & k_1 > 0 \cup (k_1 = 0 \cap \\ & (k_2 > 0 \cup (k_2 = 0 \cap k_3 > 0)) \\ \hat{\mathbf{u}}^*(-\mathbf{k}) & other \end{cases}, \tag{2}$$

where α and β are two randomly picked real vectors, $k = |\mathbf{k}|$ and $\hat{\mathbf{u}}^*$ is the complex conjugate of $\hat{\mathbf{u}}$. In the above formulation, the cross

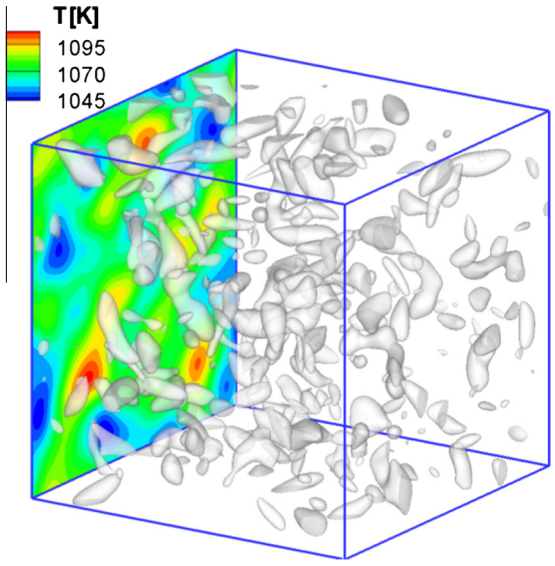

Fig. 1. The initial temperature and turbulence field used in the 3D DNS. The rotational structures are visualized using the λ_2 method [20].

product with k is to satisfy the divergence-free constraint. For $E(k)$, the 3D version of energy spectrum of Passot–Pouquet [9] (following [3]) is used:

$$E(k) = 16\left(\frac{2}{\pi}\right)^{1/2} k^4 \exp(-2k^2). \tag{3}$$

The fluctuating temperature field is similarly generated except the cross product with k is removed. The turbulence integral scale is set to 1 mm and the root mean square (rms) turbulent velocity fluctuation is $u_0' = 0.5$ m/s. For the initial temperature field, the integral scale is 1.32 mm and the rms is $T_0' = 15$ K. The turbulent Reynolds number based on integral scale is $Re_L = 144$ and the Kolmogorov scale η is around 24 μm which is resolved by three grid cells. Based on the above condition the homogenous ignition delay time calculated using Li et al. mechanism [27] is $\tau_0 = 3.3$ ms (it is 3.0 ms with an older chemical kinetic mechanism [3]) and the maximum heat release rate is $HR_0 = 2.94 \times 10^{10}$ J/m^3/s. The initial 3D temperature and flow field is shown in Fig. 1, where the turbulence rotational structures are visualized using the λ_2 method [30].

To alleviate the influence due to the randomness in the initial field and the usage of different DNS solver than those in [2–7] (where a full-compressible solver was used), we performed two additional 2D-DNS runs using our DNS solver. The 2D setup is the same as in [3] except the grid resolution. One case runs on a 512^2 grid, i.e. with the same grid resolution as the 3D-DNS. The other case runs on a 1024^2 grid with finer resolution, which is comparable to the 960^2 grid used in [3]. For all the DNS cases in this paper the computational time step was set to 1 μs and the total simulation duration is 4 ms. For solving the Poisson equation parallelly with Multigrid method the data synchronization was implemented at all grid levels, therefore an 10^{-6} error drops is achieved within 30 V-cycles[25,31]. The 3D-DNS case takes 2048 processor cores (2.1 GHz) in a Cray cluster running for 15 days.

3. Results and discussions

3.1. Numerical diagnostic tools and 1D test runs

Following [3], a reaction front is defined as the iso-surface of the a chosen value of H_2 mass fraction ($Y^c_{H_2} = 8.5 \times 10^{-4}$), the displacement speed of this front is defined as

$$S_d = \left(-|\nabla Y_{H_2}|^{-1} \frac{D}{Dt} Y_{H_2}\right)_{Y^c_{H_2}}. \tag{4}$$

Using the conservation equation of species mass, the material derivative of H_2 mass fraction ($\frac{D}{Dt}Y_{H_2}$) can be written as:

$$\frac{D}{Dt} Y_{H_2} = \frac{1}{\rho} \nabla \cdot (\rho D_{H_2} \nabla Y_{H_2}) + \frac{\dot{\omega}}{\rho}, \tag{5}$$

where the first term on the right-hand side (r.h.s) represents the contribution from molecular diffusion while the second term represents the contribution from chemical reactions (also referred as diffusion budget term and reaction budget term, respectively). D_{H_2} is the diffusivity of H_2, ρ is the density of the gas mixture, and $\dot{\omega}$ is the net reaction rate of H_2. To exclude the influence of heat release on the displacement speed, the density weighted front speed is defined as

$$S_d^* = \frac{\rho}{\rho_0} S_d, \tag{6}$$

where ρ_0 is a representative density of assumed unburned reactants.

To investigate the structures and propagation of the ignition front it is useful to start with a one dimensional test problem. Chen et al. [3] performed a parametrical study with 1D test runs with various initial temperature distributions. Considering a different reaction mechanism and numerical solver are used in this work, we perform similar 1D runs to the cases of Chen et al. [3]. The initial temperature distribution for all the 1D runs is presumed to be a sinusoidal wave with different wave lengths (L), whereas all cases share the same mean and rms temperature as the 3D case to be reported below. Figure 2 shows the computed evolution of S_d^* from the three 1D runs with lengths L of 4.1, 1.5 and 0.75 mm, respectively. Similar to the results reported in [3], all S_d^* curves are of the "U-shape" which represents a stabilized low speed front propagation embedded in between the first ignition and final stage of fuel consumption, both happening at unbound speeds occurring at spatial locations with zero fuel gradient. With decreasing L, the onset of the ignition front is delayed and the total ignition duration becomes shorter. The lowest S_d^* during the ignition process, shown in the figure as the bottom part of the U-curve, varies with L with the lowest value found at $L = 1.5$ mm. Figure 2 are similar to Fig. 3a in [3] quantitatively. The lowest S_d^* value at $L = 0.75$ mm corresponds well to the "diffusive limit" speed ($S_L = 0.5$ m/s) shown in Fig. 3 in [3], which was used in [3] to discriminate the reaction fronts between deflagration and spontaneous ignition waves.

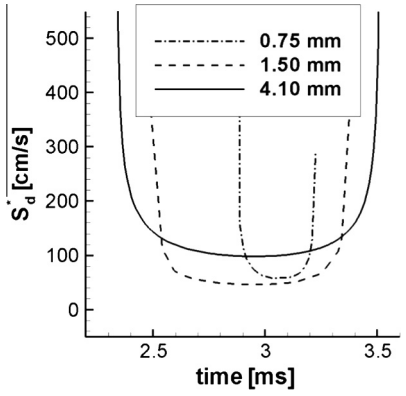

Fig. 2. The density weighted displacement speed S_d^* conditioned on $Y_{H2} = 8.5 \times 10^{-4}$ computed from the three 1D cases ($L = 4.1$, 1.5 and 0.75 mm).

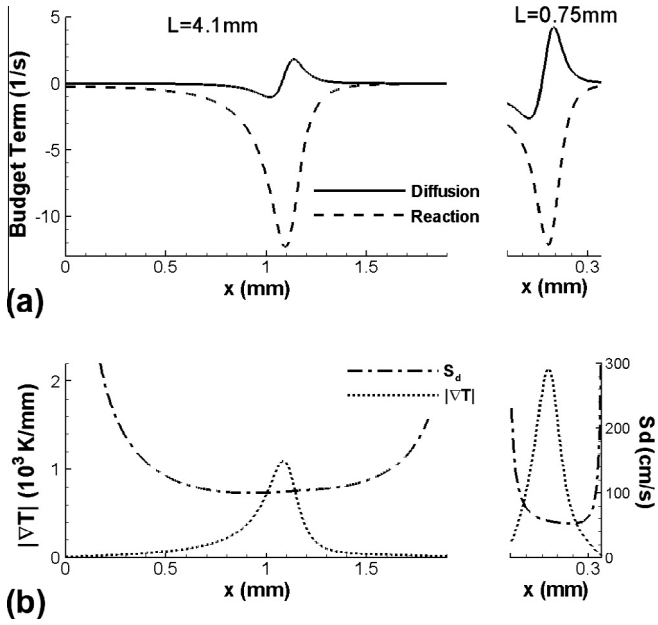

Fig. 3. Spatial distributions of the budget terms from diffusion and reactions (a), and the temperature gradient and the density weighted displacement speed conditioned at local Y_{H2} value (b), for two 1D cases (L = 4.1 and 0.75 mm). The profile is plotted at 3 ms, corresponding to the low part of the "U-shape" curve in Fig. 2.

The structures of the propagating front can be examined by plotting the spatial distribution of the terms involved in S_d^* formulation (i.e. Eq. (6)). Figure 3a shows the profiles of two budget terms from the diffusion and the chemical reactions from two 1D runs (L = 4.1, 0.75 mm) near the bottom of the U-curve, whereas the corresponding profile of temperature gradient is shown in Fig. 3b. Different from the case of L = 0.75 mm where the reaction rate budget term is balanced by the diffusion budget term, for the case L = 4.1 mm the reaction rate term dominates over the diffusion term, which is also accompanied by a lower magnitude of local temperature gradient. This corresponds to the well-known difference between the deflagration front and the spontaneous ignition front. Figure 3 can be well compares to Fig. 4 in [3]. It can also be seen from Fig. 3 that the least thick temperature gradient profile has a 200 μm thickness ($L_{|\nabla T|}$, defined as the distance in between the two points of 5% of peak temperature gradient value), which can be sufficiently represented by 25 cells under the DNS grid resolutions. It may also be useful to point out a rough estimation of the reaction front frequency (estimated as $S_d^*/L_{|\nabla T|}$) is around 2.5 kHz, which is two order magnitude smaller than 160 kHz of the base acoustic frequency (estimated as the sound speed divided by the domain size, with sound speed around 655 m/s at T_0), this supports the usage of low Mach number assumption with which flame/acoustic interaction can be neglected.

Figure 3b also shows the spatial profiles of S_d^* with the conditioned $Y_{H_2}^c$ value replaced with the local Y_{H_2} value. It can be seen that S_d^* remains rather constant at the middle zone where the

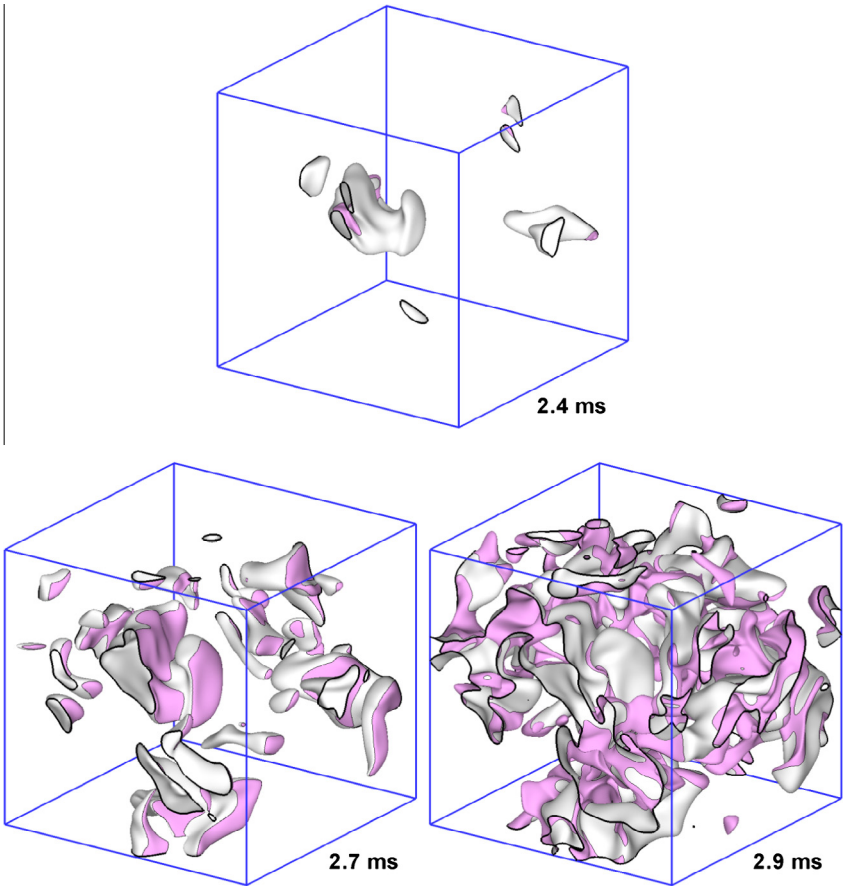

Fig. 4. Three-dimensional instantaneous front surfaces (defined at $Y_{H2} = 8.5 \times 10^{-4}$) at 2.4, 2.7 and 2.9 ms. The grey shadow denotes the slow deflagration front ($S_d^* \leqslant 1.1 \cdot S_L$) while purple shadow represents the spontaneous ignition front ($S_d^* > 1.1 \cdot S_L$). Note that the black lines are the reaction fronts intersecting on the boundaries of the computational domain.

reaction is intense. Therefore, for later discussion in this paper we use the same conditioned value $Y^c_{H_2} = 8.5 \times 10^{-4}$ as in [3], which approximately corresponds to maximum heat release point.

3.2. Instantaneous 3D deflagration and spontaneous reaction fronts

The 1D study shows that under the present HCCI conditions the reaction front is initiated as spontaneous ignition wave, followed by deflagration wave propagation. In [3] the deflagration fronts are discriminated from the spontaneous ignition fronts according to the criterion that $S^*_d < 1.1 \cdot S_L$. Considering the similarity of the present 1D runs with those in [3], the same criterion is adopted in this work. Figure 4 shows three instantaneous 3D reaction fronts at t = 2.4, 2.7 and 2.9 ms, where t = 0 corresponds to the initial field. The front surface is colored to distinguish the deflagration front from the spontaneous ignition front. As seen from the figure the front surfaces are well resolved in the 3D-DNS. At the three instance of time shown in the figure, there exist multiple disconnected reaction fronts in the domain. The creation of these regions is most likely due to spontaneous auto-ignition of the local hot spots. The growth of the already ignited spots due to the combined propagations of deflagration and ignition fronts, together with the new front surface from ignition, leads to a rapid increase in the total front surface area.

It can be seen that during early ignition (2.4 ms) most of the reaction front propagates as a slow deflagration wave, with small portion of the reaction front propagating as the fast ignition wave, e.g. around the sharp tip region of the ignited spots. At 2.7 ms the fraction of ignition front within the total reaction front becomes larger, and at 2.9 ms the area of the fast ignition fronts are comparable to that of the slow deflagration fronts. The above observation suggests that the averaged front speed is increasing during 2.4–2.9 ms, which will be verified later.

Figure 5 shows a 2D snapshot of HO_2 mass fraction (Y_{HO2}) at 2.8 ms, with three contour lines defined at different values ($Y_{H2} = 2 \times 10^{-4}$, 8.5×10^{-4} and 2×10^{-3}). In the 2D Y_{HO2} field there are both smoothly distributed region and region with large spatial variation. The Y_{HO2} field outside the $Y_{H2} = 2 \times 10^{-3}$ contour is quite smooth, due to the existence of considerable amount of unburned fuel and a relatively slower reaction rate. The rapid reaction region in between $Y_{H2} = 2 \times 10^{-4}$ and $Y_{H2} = 2 \times 10^{-3}$, however, shows

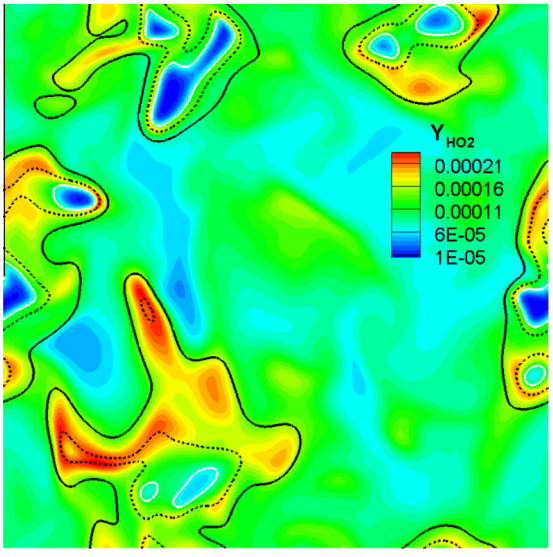

Fig. 5. An instantaneous Y_{HO2} distribution in the cross-sectional plane through mid-z coordinate at 2.8 ms. The contour lines are defined at three Y_{H2} values: 2×10^{-4} (white), 8.5×10^{-4} (dash, black) and 2×10^{-3} (black).

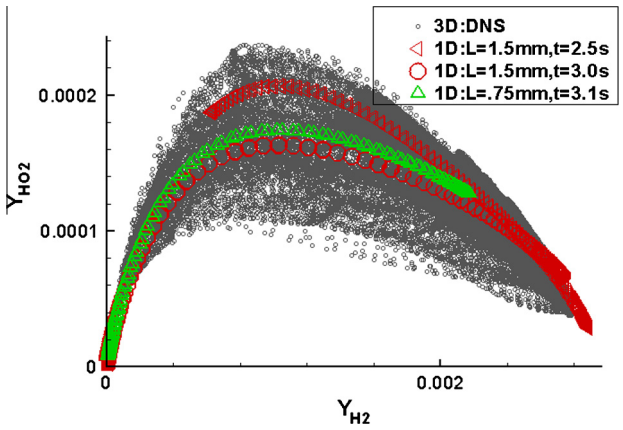

Fig. 6. A scatter plot in Y_{HO2}–Y_{H2} space over the same cutting plane of the 3D case in Fig. 5, as well as from the 1D runs shown in Figs. 2 and 3.

rather large spatial variation of Y_{HO2}. Close to the reaction front ($Y_{H2} = 8.5 \times 10^{-4}$) there are several regions with sharp gradient of Y_{HO2}. On the other hand, in certain regions around the reaction front rather low smooth distribution of Y_{HO2} can be found, which suggests a weak correlation between the HO_2 and H_2 species This can also be verified in Fig. 6, a scatter plot of Y_{HO2} verse Y_{H2} over the same plane, in which large scattering of Y_{HO2} can be seen in the middle range of possible Y_{H2} value. The weak correlation between the two species indicates the importance of using detailed chemistry mechanism and resolving all detailed transport equations for an accurate prediction of the ignition process.

According to the Zel'dovich theory [1], the displacement speed of a fast spontaneous propagation front is inversely proportional to the local temperature gradient. 2D-DNS results of Chen et al. confirmed such relation [3]. This relation is verified using the present 3D-DNS results as well. Figure 7 shows the correlation of S^*_d with $|\nabla T|$ at the reaction front (defined at $Y_{H2} = 8.5 \times 10^{-4}$) in a logarithmic scale at 2.7 ms. A lower temperature gradient yields a faster displacement speed that can reach a few hundreds meters per second. The 2D-DNS results of Chen et al. [3] suggested that the displacement speed for the slow deflagration front is weakly sensitive to temperature gradient; this is confirmed in the present 3D-DNS results, e.g. the inset of Fig. 7 showing for $|\nabla T| \geqslant 1800$ K/mm. S^*_d decreases with increasing temperature gradient and it approaches a limiting value, about $0.2S_L$.

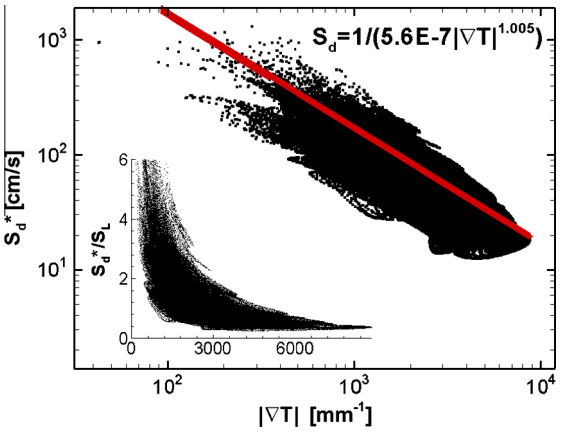

Fig. 7. Correlation of the displacement speed (S^*_d) against temperature gradient ($|\nabla T|$) on the reaction front surface in log-scale at 2.7 ms. The inset figure is plotted at regular scale. The power-fit line with an exponent of −1.005 is from the 2D DNS data of Chen et al. [3].

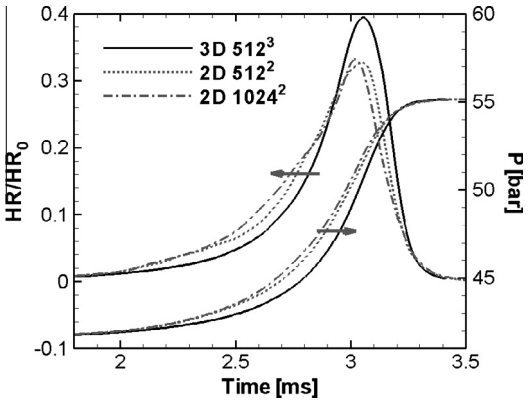

Fig. 8. Pressure trace and the normalized heat release rate (HR/HR_0) from the 3D-DNS and 2D-DNS cases.

3.3. Comparison between 2D and 3D DNS

Figure 8 shows the thermodynamic pressure in the domain and the evolution of the volumetric heat release rate from the 3D-DNS and 2D-DNS. The heat release rate is normalized with HR_0. The main ignition events in all cases, defined at the instance of time of the highest heat release rate and the largest pressure rise rate, are found around 3.05 ms. Due to the randomness in the initial condition and the use of different grid resolutions the results from the two 2D runs are slightly different; the peak values of the heat release rate from the two 2D cases are around $0.33HR_0$, which can be compared to the value of $0.34HR_0$ reported in [3].

Compared with the 2D results the 3D-DNS results show a delayed ignition, and a more rapid heat release with a higher peak value of $0.40HR_0$, about 15% higher than the 2D predications. Similar observation can be seen in the pressure profiles. It should be noted that the fuel in all cases is fully burned after 3.5 ms.

The temporal evolution of the mean displacement speed (S_d^*) averaged over the entire reaction fronts from 2D- and 3D-DNS is displayed in Fig. 9. Consistent with the results of [3], all 2D- and 3D-DNS runs predict an overall "U-shape" curve similar to the 1D runs. After the early ignition stage the mean displacement speed falls to around S_L (0.5 m/s, e.g. from 2.2 ms to 2.6 ms), indicating that the overall reaction fronts propagate likely as deflagration waves. Thereafter, S_d^* increases to 2 m/s at 3.2 ms and then drops slightly before a rapid increase, which lasts until the end of fuel consumption in the domain. This observation is consistent with the 3D reaction front structures shown in Fig. 4. The S_d^* values in the middle part of the "U-shape" between 2D and 3D are rather similar, which can be attributed to the similar level of 2D and 3D mean temperature gradient developed prior to the ignition onset (later shown in Fig. 11a at 1.5 ms). It can also be noticed in Fig. 9 that the onset of ignition in 3D-DNS occurs earlier (at 1.8 ms) than that in 2D-DNS (at 2.1 ms). Since the area of the early ignition fronts is small, their contribution to the total heat release and pressure rise is not significant, Fig. 8.

Figure 9 also shows the evolution of total reaction front area from the 2D- and 3D-DNS. To be comparable with the 3D front area, the "2D front area" is calculated as the product of the total 2D front length with the domain width (4.1 mm). It can be seen the total front area in all cases increases gradually from the beginning. After reaching a maximum value it decreases rapidly to zero. Compared with 2D-DNS, 3D-DNS predicts a slower increase of the total front area during early ignition. Later on the 3D front area increases much more rapidly; it then overtakes the 2D front area and reach to a higher maximum value at 3.05 ms (at least 10% higher than the 2D maximum values). At this instance of time the 3D heat release rate also reaches the peak value, Fig. 8. It can also be noticed that at the same instance of time S_d^* from the 3D-DNS is quite similar as the 2D one. Therefore the higher 3D peak heat release rate observed in Fig. 8 is due to the larger total front area in 3D-DNS as compared with 2D-DNS.

To understand the differences between 2D- and 3D-DNS results we examine the development of temperature field before the onset of ignition. Figure 10 shows the early evolution of normalized rms velocity (u'/u_0'), rms temperature (T'/T_0', T' defined in Appendix A) and maximum temperature ($(T_{max}-T_0)/T_0'$) within the domain from different DNS runs. It is seen that the rms velocity all decay monotonically. There is little difference between the two 2D rms velocities; however, the 3D turbulence decays much faster than the 2D ones. This implies a larger mean dissipation rate of turbulent kinetic energy (ε) in 3D, which can be verified later. For the maximum temperature, the 3D value is consistently higher than the 2D ones throughout the simulation time, which explains the earlier onset of ignition in the 3D-DNS. The difference in T_{max} is a result of the larger number of grid points (thus larger samples of

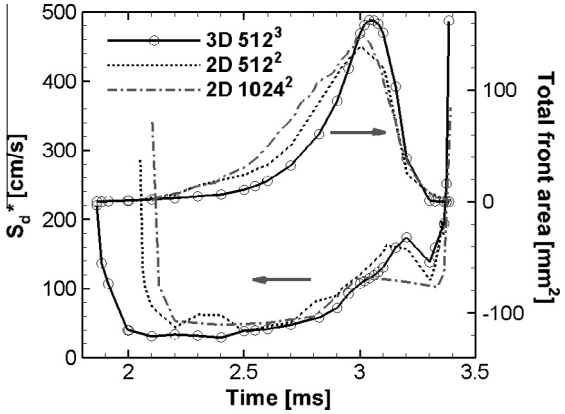

Fig. 9. Reaction front area averaged displacement speed (S_d^*) and total reaction front area from the 3D-DNS and 2D-DNS cases. Note that the 2D front area is calculated as the product of the 2D front length and the domain width (4.1 mm).

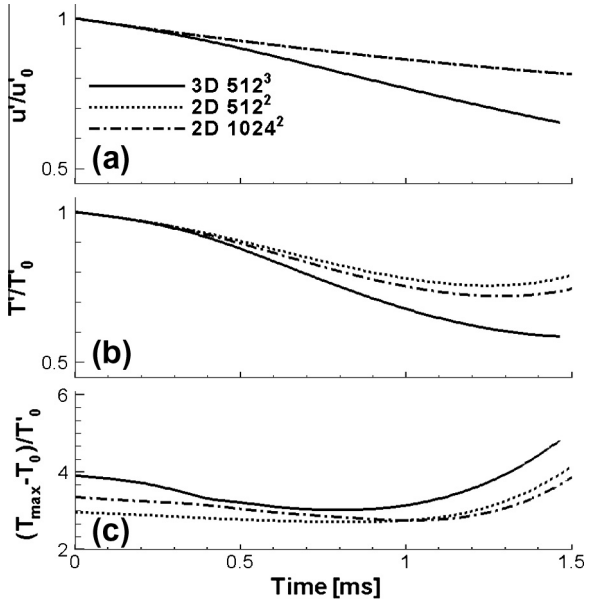

Fig. 10. Normalized rms velocity (u'/u_0', (a), rms temperature (T'/T_0', (b) and maximum temperature ($(T_{max}-T_0)/T_0'$, (c) during the early ignition time from the 3D-DNS and 2D-DNS cases.

realization) in generation of the 3D initial random temperature field.

During the early evolution (before 1.3 ms) T' decreases monotonically in time owing to turbulent mixing. Compared with the 2D-DNS runs the 3D-DNS predicts a faster decay of T', which leads to a more homogenous 3D temperature field prior to the onset of ignition. Since the averaged temperatures from all cases evolve very similarly at the early stage (observed from the DNS data, not shown here for brevity), higher stratification in the 2D temperature field leads to a larger fraction of hot gas for an early spontaneous ignition which contributes to the earlier heat release and pressure rise in 2D-DNS than in 3D-DNS, as observed in Fig. 8. Being relatively delayed in the bulk heat release the more homogenous 3D field, when ignited, tends to burn more rapidly with a higher overall fuel consumption rate and higher heat release rate. It is worth mentioning that the higher heat release rate in 3D-DNS is due primarily to the larger total front area in 3D, rather than a faster 3D front speed.

To explain the observed faster T' decay in the 3D case, we derived the evolution equation of T'^2 (Eq. (A3) in the appendix, for the case of constant density field). It is clear that the decreasing rate of T'^2 is mainly due to the mean temperature gradient magnitude $\langle|\nabla T|^2\rangle$ (where operator $\langle\rangle$ denotes spatial average), cf. Fig. 11a. Starting with the same value from the initial random fields, $\langle|\nabla T|^2\rangle$ in all 2D and 3D cases raises to a peak and then it decreases monotonically. Compared with all 2D ones, the 3D $\langle|\nabla T|^2\rangle$ has a faster early increase and it also reaches to a higher peak value. It is interesting to notice a "confliction" that prior to ignition (at 1.5 ms) the 3D mean temperature gradient is similar as the 2D one although the 3D T' is much smaller than the 2D one, which is allowed due to the extra space dimension. As shown by Eq. (A4), the evolution of $\langle|\nabla T|^2\rangle$ is governed by a dissipation term and a mean production term $\langle P_{|\nabla T|}\rangle$. Since the dissipation term is negative, the faster increase of 3D $\langle|\nabla T|^2\rangle$ must be driven by a larger positive $\langle P_{|\nabla T|}\rangle$ in 3D. From Eq. (A6), $\langle P_{|\nabla T|}\rangle$ can be written as a multiplication of three terms with the mean temperature gradient ($\langle|\nabla T|^2\rangle$), mean velocity strain $\left(\langle S_{ij}^2\rangle^{1/2}\right)$ and a normalized production term $\left(\left\langle\widehat{P_{|\nabla T|}}\right\rangle\right)$. The evolution of the remaining two terms is also shown in Fig. 11. It can be seen that while $\langle\widehat{P_{|\nabla T|}}\rangle$ evolves similarly for all cases, the evolution of the mean strain rate differs significantly between 2D and 3D. Starting with an initially higher value (3/2 times of the 2D one), the 3D mean strain first rises before later dropping, which is also different from the monotonic decrease of the 2D strain rate. The 2D/3D difference can then be attributed to a combined effect of higher initial value and additional rise of the 3D strain rate.

The larger initial 3D strain is a result of one extra spatial dimension than the 2D cases. Since both the initial turbulence integral scale and integral velocity are set equal for the 2D and 3D DNS runs, the mean turbulent kinetic energy is larger in 3D ($k_{3D} = \frac{3}{2}u'^2$) than in 2D ($k_{2D} = u'^2$). The same is true for the mean kinetic energy dissipation rate (ε), which scales with the mean strain rate ($\varepsilon \equiv 2\upsilon\langle S_{ij}^2\rangle$ under homogenous turbulence, where υ is the dynamic viscosity).

The early rise of 3D mean strain rate is also due to the extra dimension. This can be understood by examining the evolution equation of mean strain rate (Eq. (A9), also seen in Eq. 3.204 in [32]), which contains a negative dissipation term and a production term due to the strain-self-amplification term $\left(-\frac{2}{3}\langle S_{ij}S_{ik}S_{jk}\rangle\right)$. The production term in 3D turbulence tends to be positive (see Eq. 3.208 in [32]), however it is zero in 2D (trivial to prove).

To summarize, the extra dimension in 3D causes a higher initial mean strain rate and also a positive production term of the mean strain rate, which leads to an additional generation of the temperature gradient and consequently a quicker mixing of temperature field (faster heat transfer), resulting in a delayed but more rapid ignition of bulk mixture in 3D cases. It is interesting to note that the vortex stretching mechanism, responsible for the 2D/3D difference in turbulence energy cascading, does not play an explicit role in creating the above observed difference. Furthermore the faster 3D ignition is mainly achieved through larger 3D flame area instead of mean front displace speed which is similar between 2D and 3D. For a better mixed 3D temperature field (lower T'), the extra space dimension in 3D also allows the existence of similar mean temperature gradient as in 2D.

3.4. The front stretch and characterization of 3D reaction front surface

As shown in the above discussion the ignition of bulk mixture is achieved through a continuous change of total reaction front area. It will be of interest to examine the stretch of the 3D reaction front.

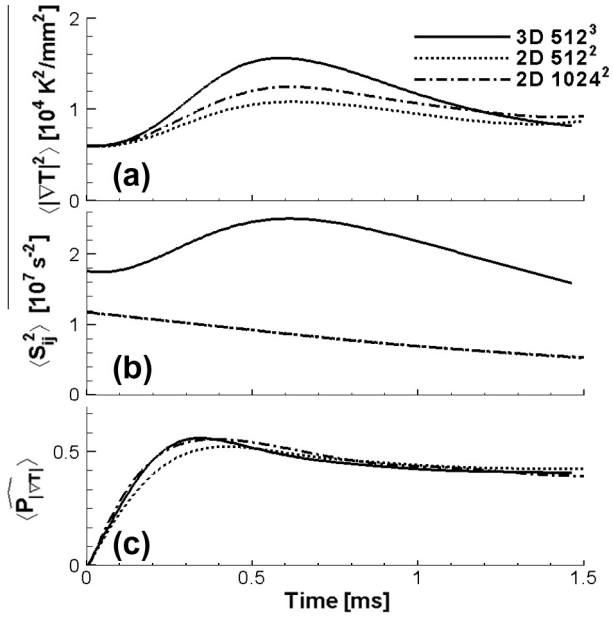

Fig. 11. Volume-averaged mean temperature gradient square ($\langle|\nabla T|^2\rangle$, (a), square of the velocity strain rate ($\langle S_{ij}^2\rangle$, (b), and the normalized production term ($\langle\widehat{P_{|\nabla T|}}\rangle$, (c) during the early ignition time from the 3D-DNS and 2D-DNS cases.

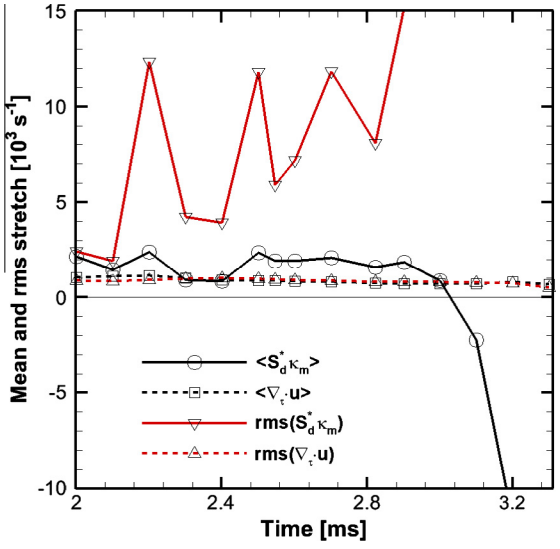

Fig. 12. Evolution of the mean and rms of the strech induced by curvature ($S_d^*\kappa_m$) and the strech due to the tangential strain rate ($\nabla_\tau \cdot \boldsymbol{u}$).

Figure 12 shows the evolution of mean and rms of the front stretch induced by curvature ($S_d^*\kappa_m$, where κ_m is the mean curvature of a local 3D surface) and the tangential strain ($\nabla_\tau \cdot \mathbf{u}$, ∇_τ is the tangential projection of gradient operator and u is the velocity vector). The mean and rms for a given stretch part ($\mathbb{k}$) are defined respectively as

$$\langle \mathbb{k} \rangle = \int_s \mathbb{k}\, dA \Big/ \int_s dA, \tag{7}$$

and

$$\mathbb{k}' = \left(\int_s (\mathbb{k} - \langle \mathbb{k} \rangle)^2 dA \Big/ \int_s dA \right)^{1/2}, \tag{8}$$

while dA represents the elements on the entire reaction front S. The mean and rms of the tangential strain rate are similar in magnitude; both quantities are rather constant throughout the ignition process, indicating a statistically steady effect by the flow turbulence. The positive mean tangential strain rate may be attributed to the heat release effect for pockets burning overall outward. For the curvature-induced stretch, the mean value changes from positive to negative as ignition proceeds, similar trend was also shown in Fig. 16 for the 2D-DNS in [3]. Compared to the mean curvature-induced stretch, the mean tangential strain seems to contribute a non-negligible portion of early growth the total front area, as shown in Fig. 12 from 2.0 to 2.9 ms. This observation may imply that, in addition to the diffusion effect (as pointed out in [3]) which results in the reaction front propagation, the flow convection effect should also considered if an accurate prediction of ignition process is required. This can be useful for evaluating the modeling approaches (such as the multizone model studied in [3]) in which both the diffusion and convection effects are neglected.

It can be seen in Fig. 12 that the rms of curvature-induced strain is much higher than the rms of tangential strain during most of the ignition process. The larger variation in curvature-induced stretch can also be seen in Fig. 13 which shows a scatter-plot of the curvature-induced stretch verses the tangential strain at 2.8 ms, colored by the jointed PDF. Both mean values are also plotted as reference. Compare to the tangential strain the curvature-induced stretch has much wider spreading away from the mean value and skews to the positive side. The large variation in curvature-induced stretch is related to the broad range of local curvature values computed from the complicated 3D front surface (as shown in Fig. 4 of the instantaneous reaction fronts). It is useful to categorize the surface elements according to the topological features and then quantify their contributions to the reaction front propagation. The curvature of the reaction front surface, which can affect both the deflagration and ignition front propagation, is examined.

A 3D surface element can always have two real-valued principal curvatures, κ_1 and κ_2. The 3D mean curvature can be represented as the average of the two principal curvatures, i.e. $\kappa_m = (\kappa_1 + \kappa_2)/2$. The Gaussian curvature is defined as the product of the two curvatures, i.e. $\kappa_g = \kappa_1\kappa_2$. The mean curvature denotes the averaged concaveness/convexness of the local surface. For the Gaussian curvature, a positive κ_g means a "spherical" surface (κ_1 and κ_1 have the same sign) and a negative κ_g denotes a "saddle" surface (κ_1 and κ_1 have different signs). While concaveness and convexness can also be used to characterize the 2D ignition surface, the saddle surface is an exclusive 3D feature. Figure 14 shows a scatter-plot of κ_g and κ_m for all the surface elements on the reaction front at 2.7 ms, colored by the joint population density function (PDF) in logarithmic scale. Close to the center region (small $|\kappa_g|$ and $|\kappa_m|$) the reaction fronts are mostly flat surfaces. The population density skews towards the positive κ_m indicating that the fronts are overall convex to the unburned mixture, since most reaction kernels at this moment grow outwards. The surface elements at the top right region ($\kappa_g \gg 0$, $\kappa_m \gg 0$) are due to the newly formed ignition spots, which tend to be small convex spheres. As seen in Fig. 14 all possible elements on the reaction fronts lie on or below a parabola ($\kappa_g = \kappa_m^2$), which is the mathematical bound for preventing non-real solution of principal curvature. On the parabola the local front element is a perfect spherical surface with two equal principal curvatures, $\kappa_1 = \kappa_2$.

A 2D reaction front is seen as the horizontal dashed line in Fig. 14 ($\kappa_g = 0$, as one of principal curvature is zero). Such 2D surfaces, e.g. cylinders, separate the curvature space into two regions, the spherical like surface region with $\kappa_g > 0$ and the saddle surface region with $\kappa_g < 0$. The saddle surfaces occupy 45% of the total surface area of reaction front at 2.7 ms.

The curvature features of 3D surface elements can also be quantified using the shape factor [33–35] which is defined as $S_h = \kappa_{min}/\kappa_{max}$, where κ_{min} and κ_{max} are respectively the smaller or larger one between κ_1 and κ_2. The S_h value can only vary between -1 and $+1$. $S_h = 0$ refers to the cylindrical surface element ($\kappa_g = 0$) while $S_h = \pm 1$ represents respectively a perfect spherical region or a perfect spherical saddle region. Figure 15 shows the PDF plot of

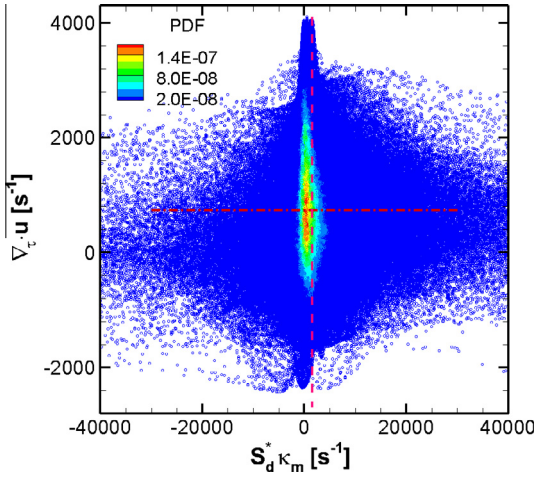

Fig. 13. Correlation of the curvature-induced stretch ($S_d^*\kappa_m$) with tangential strain rate ($\nabla_\tau \cdot \boldsymbol{u}$) on the reaction front surface at 2.8 ms, colored by the joint PDF. The horizontal/vertical dash line corresponds respectively to the mean curvature-induced stretch $\langle S_d^*\kappa_m \rangle = 1578\ s^{-1}$ and mean tangential strain rate $\langle \nabla_\tau \cdot \boldsymbol{u} \rangle = 733\ s^{-1}$, as shown in Fig. 12.

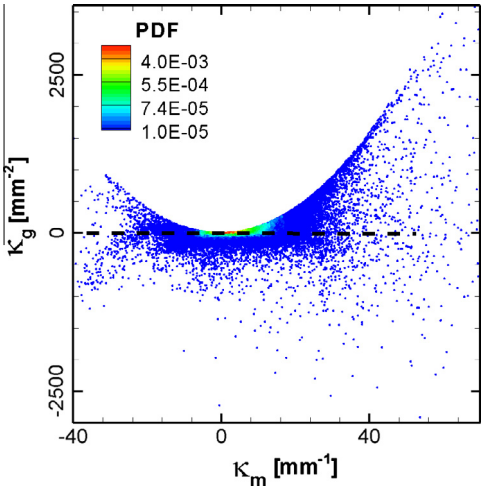

Fig. 14. Correlation of the mean curvature (κ_m) with Gaussian curvature (κ_g) on the reaction front surface at 2.4 ms, colored by the joint-PDF. The dash line with $\kappa_g = 0$ represents the 2D-like cylindrical surfaces.

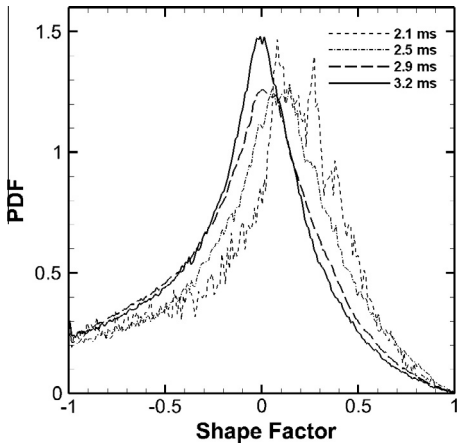

Fig. 15. PDF of shape factor for the 3D reaction front surfaces at four different instants (2.1, 2.5, 2.9 and 3.2 ms).

the shape factor at four different instants (2.1, 2.5, 2.9 and 3.2 ms). With time the shape factor changes towards the negative direction, indicating the increasing percentage of saddle regions. The zero probability converged at $S_h = 1$ indicates it is impossible to find perfect spherical surfaces, however there exist some probability finding perfect spherical saddle surface at $S_h = -1$. Similar observations can be found in [34].

The non-zero possibility at $S_h = 1$ observed at Fig. 15 may be contributed by those weak saddle regions of overall flat surface ($|\kappa_m| \approx 0$) and with two small principle curvatures of different sign ($\kappa_1 = \kappa_2 \approx 0$). It will be more interesting to study stronger saddle surface element. To be specific, one may introduce a cutoff Gaussian curvature, $\kappa_{g,c} = 44.35\ \text{mm}^{-2}$ and define the strong saddle (SA) region with $\kappa_g < -\kappa_{g,c}$. This cutoff value is chosen in such a way that the SA surfaces occupy about 2% of the total reaction front area at 2.7 ms. Similarly, we define a small sphere (SP) region with $\kappa_g > \kappa_{g,c}$. In case of a perfect spherical surface elements, $\kappa_{g,c}$ corresponds to a sphere with a radius of 0.15 mm.

Figure 16 shows the fraction of the total front area occupied by the SA (f_{sa}) and SP fronts (f_{sp}), the fraction of total fuel consumption rate by the two fronts (m_{sa} and m_{sp}), and the fraction of the curvature-induced front stretch by the two fronts (K_{sa} and K_{sp}). These quantities are defined as follows

$$
\begin{aligned}
f_{sa} &= \int_s dA_{sa} \Big/ \int_s dA, \\
m_{sa} &= \int_s S_d^* \cdot dA_{sa} \Big/ \int_s S_d^* \cdot dA, \\
K_{sa} &= \int_s s_d^* \cdot \kappa_m \cdot dA_{sa} \Big/ \int_s s_d^* \cdot \kappa_m \cdot dA,
\end{aligned}
\tag{9}
$$

where dA_{sa} represents the surface elements on the SA front. f_{sp}, m_{sp} and K_{sp} are defined similarly.

During the entire ignition the SA surfaces occupy a small fraction of the total reaction front area (2–6%), it however contributes to 4–10% of the total fuel consumption. The almost doubled contribution in fuel consumption than in area suggests that the overall SA fronts propagate with twice of the mean front displacement speed. This observation may be explained considering the saddle surfaces are likely to be inherited from the high temperature isosurface around an initially unburned hot pocket, or generated during merging of two nearby ignited spots. Both events are faster than the propagation of the slow, undisturbed deflagration front.

Figure 16b shows that the SP area fraction (f_{sp}) decreases from 15% to 3% from 2.0 to 3.1 ms. At the later time, a rapid increase of f_{sp} is because most of unburned reactant pockets approaching

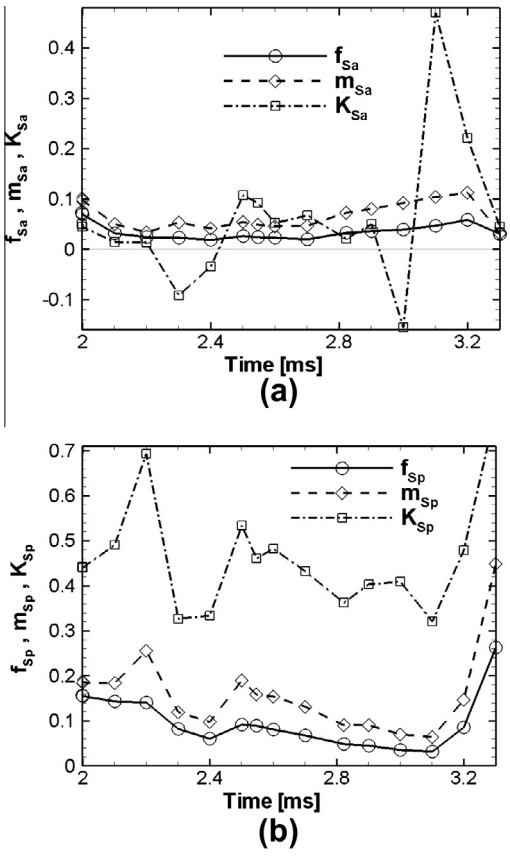

Fig. 16. Fraction of total reaction front area (f), fuel consumption rate (m) and curvature-induced stretch (K) contributed by the strong saddle fronts (a: f_{Sa}, m_{Sa}, K_{Sa}) and small spherical fronts (b: f_{Sp}, m_{Sp}, K_{Sp}).

the end of combustion tend to become small spheres. Compared with the SA fronts, the SP fronts are more abundant during the earlier combustion stage (before 2.9 ms); this may be explained by the production of SP surfaces from newly formed spontaneous ignited spots (corresponding to spreading to the top-right corner of Fig. 12). As the ignition proceeds the increase in the total front area comes more from the growth of the already ignited spots (as seen in Fig. 4), the f_{sp} decreases, and at 3.1 ms f_{sp} becomes even lower than f_{sa}. The high front displacement speed related to the spontaneous ignition wave at the SP surfaces can also explain the observed higher fraction in the fuel consumption rate (7–25%) than the area fraction. From 2.7 ms to 3.1 ms, the SA and SP fronts defined by the cutoff $\kappa_{g,c}$ together contribute to about 8% of total reaction front area and about 16% of the total fuel consumption.

Figure 16a shows that the fraction of curvature-induced stretch from the SA fronts (K_{Sa}) oscillates across zero. From 2.3 ms to 2.5 ms K_{Sa} changes from −9% to +11%, while from 3.0 ms to 3.1 ms it changes from −18% to 48%. It should be pointed out that before 3.1 ms the total curvature-induced stretch is positive, and it changes sign later on. Different from the SA fronts the SP fronts contribute to the positive stretch, Fig. 16b. During the middle auto-ignition (2.6–2.9 ms) the SP fronts are responsible for around 40% of the total curvature-induced stretch, which is much higher than the contribution by the SA fronts.

Figure 17 shows the mean curvatures averaged over the SA and SP fronts, i.e. $\langle \kappa_m \rangle_{Sa}$ and $\langle \kappa_m \rangle_{Sp}$. Both curvatures change from an early positive value to a later negative value. Approaching the end of combustion the reaction fronts will be mostly concave to consume the remained reactants pockets, which leads to negative mean curvatures. Before 2.9 ms, a major part of the SP fronts are

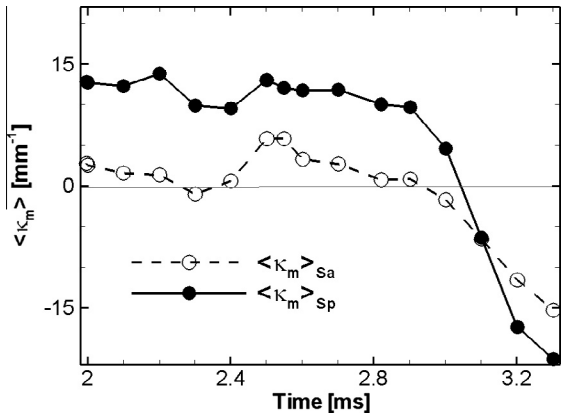

Fig. 17. Mean curvatures averaged over the strong saddle fronts $\langle\kappa_m\rangle_{Sa}$ and the small spherical fronts $\langle\kappa_m\rangle_{Sp}$.

highly curved convex surfaces ($\langle\kappa_m\rangle_{Sp} > 10\,\mathrm{mm}^{-1}$). This explains the above observed large stretch contribution. Compared with the SP fronts the SA fronts are overall flatter ($|\langle\kappa_m\rangle_{Sa}| < |\langle\kappa_m\rangle_{Sp}|$), which explains the relative small contribution from the SA surface to the curvature induced stretch before 3.0 ms. Figure 17 shows that most of SA fronts turn to be concave at 3.0 ms, which is 0.1 ms earlier than the SP fronts. Since the total stretch also changes sign at 3.1 ms, this leads to the cross-zero change in the SA contributed stretch from 3.0 to 3.1 ms, Fig. 16a. The other cross-zero change around 2.3 ms is also related with a sudden appearance of reaction fronts with negative $\langle\kappa_m\rangle_{Sa}$, which may be caused by a rapid creation of concave saddle fronts due to merging of random ignited spots. It is worth noting that at 3.1 ms the combined SP and SA fronts contribute to about 80% of total front reduction with only 8% of total front area.

4. Summary and conclusions

2D- and 3D-DNS are performed to study the auto-ignition of a lean H_2/air mixture with temperature stratification under a constant volume condition. The simulations are carried out using an in-house DNS solver employing detailed chemistry and transport properties. Both deflagration and spontaneous ignition fronts are identified and the correlation between the local front displacement speed and the temperature gradient is verified. Compared with 2D-DNS, 3D-DNS predicts a delayed but more rapid heat release rate (15% higher in peak value). The difference is due to that, compared with 2D turbulence, 3D turbulence yields a faster heat transfer rate that leads to a more homogenous temperature field prior to ignition. The faster heat transfer rate in 3D is a consequence of one extra spatial dimension. The extra dimension causes both a higher value of initial velocity strain rate and an additional strain-self-amplification, which then leads to a faster production of temperature gradient and quicker mixing of the temperature field. It is also found that the higher 3D peak heat release rate is mainly achieved through the larger total front area in 3D-DNS, while the mean propagation speed of reaction front is similar in 3D and 2D. The extra dimension also allows a better mixed 3D temperature field to have similar temperature gradient as in 2D.

The geometrical features of the instantaneous 3D reaction fronts are examined based on the mean and Gaussian curvatures on the local surfaces. By introducing a cutoff Gaussian curvature value two types of 3D surface elements are identified: a strong saddle front and a small sphere front. The two types of fronts occupy a small fraction of the total front area (e.g. 8%); however, they contribute to 16% of the total fuel consumption, due to the fast overall displacement speed at both fronts. During early ignition most of the spherical fronts are highly curved concave surfaces, therefore the small spherical fronts contribute to a large fraction of the total flame stretch (>30%). The strong saddle fronts are earlier in changing convex to concave and they play a more important role in reduction of reaction front area in the later stage of the combustion process.

Acknowledgments

This work was supported by the Swedish research funding organizations (CeCOST, KCFP and VR). We acknowledge PRACE for access to CURIE TN at the Très Grand Centre de Calcul (TGCC) operated by CEA. Some computations are also performed on the Lindgren cluster in PDC center of SNIC, Sweden. The authors thank reviewer's suggestions for improving the paper and also thank Félix Dabonneville for his smmer DNS work.

Appendix A. Evolution equations of mean temperature fluctuation, temperature gradient and velocity strain rate

During the early period prior to any ignition events the chemical reaction and density variation can be neglected, the evolution of the flow and scalar fields can be simplified as a mixing problem. Considering the initial uniform mixture with a rather small variation in the temperature (T) field (15 K over a temperature mean T_0 = 1070 K), the density (ρ_0), specific heat capacity of the mixture ($C_{p,0}$) and heat conductivity (λ_0) can be regarded as constant in both space and time. The evolution of the temperature field during the early period can be further simplified as a problem of mixing a passive scalar in an incompressible turbulent flow.

The governing equations for the passive mixing problem can be written as:

$$\nabla\cdot\mathbf{u} = 0, \tag{A1}$$

$$\frac{\partial T}{\partial t} + \nabla\cdot(\mathbf{u}T) = C_0\nabla\cdot\nabla T, \tag{A2}$$

where $\mathbf{u}$ is the velocity vector and C_0 is a constant as $C_0 = \lambda_0/(\rho_0 C_{p,0})$.

Based in Eqs. (A1) and (A2) and using full periodic condition, it is straightforward to derive the following exact equations describing evolution of the rms temperature and mean temperature gradient:

$$\frac{\partial}{\partial t}T'^2 = -2C_0\langle|\nabla T|^2\rangle. \tag{A3}$$

$$\frac{\partial}{\partial t}\langle|\nabla T|^2\rangle = \langle\varepsilon_{|\nabla T|}\rangle + \langle P_{|\nabla T|}\rangle. \tag{A4}$$

where the mean operator $\langle\rangle$ represents spatial averaging over the entire domain and the rms temperature is define as $T' = \langle(T-T_0)^2\rangle^{1/2}$. The two terms in the right hand side (r.h.s) of Eq. (A4) are a negative dissipation term ($\varepsilon_{|\nabla T|}$) and a strain-production term ($P_{|\nabla T|}$), respectively:

$$\varepsilon_{|\nabla T|} = -2C_0\Delta T\Delta T, \tag{A5}$$

$$P_{|\nabla T|} = -2\nabla T\cdot\nabla\mathbf{u}\cdot\nabla T = -2\frac{\partial T}{\partial x_i}S_{ij}\frac{\partial T}{\partial x_j}, \tag{A6}$$

where the velocity strain rate tensor is $S_{ij} = 1/2(\partial u_i/\partial x_j + \partial u_j/\partial x_i)$. The mean strain-production term can further be written as:

$$\langle P_{|\nabla T|}\rangle = 2\langle S_{ij}^2\rangle^{1/2}\cdot\langle|\nabla T|^2\rangle\cdot\left\langle\widehat{P_{|\nabla T|}}\right\rangle, \tag{A7}$$

where $\widehat{P_{|\nabla T|}}$ is the non-dimensional strain production

$$\widehat{P_{|\nabla T|}} = -\frac{\partial T/\partial x_i}{\langle|\nabla T|^2\rangle^{1/2}} \cdot \frac{S_{ij}}{\langle S_{ij}^2\rangle^{1/2}} \cdot \frac{\partial T/\partial x_j}{\langle|\nabla T|^2\rangle^{1/2}}. \tag{A8}$$

The evolution equation of mean strain rate is written as: (Eq. 3.204 in [32])

$$\frac{1}{2}\frac{\partial\langle S_{ij}^2\rangle}{\partial t} = -\frac{2}{3}\langle S_{ij}S_{ik}S_{jk}\rangle + \nu\langle S_{ij}\nabla^2 S_{ij}\rangle. \tag{A9}$$

The first term in the r.h.s in the above equation is a production term due to strain-self-amplification; the second term is a viscous dissipation term. In 2D cases it is apparent that the strain-self-amplification term disappears.

Reference

[1] Y.B. Zel'dovich, Combust. Flame 39 (1980) 211–214.
[2] R. Sankaran, H.G. Im, E.R. Hawkes, J.H. Chen, Proc. Combust. Inst. 30 (2005) 875–882.
[3] J.H. Chen, E.R. Hawkes, R. Sankaran, S.D. Mason, H.G. Im, Combust. Flame 145 (2006) 128–144.
[4] E.R. Hawkes, R. Sankaran, P.P. Pébay, J.H. Chen, Combust. Flame 145 (2006) 145–159.
[5] F. Bisetti, J.Y. Chen, J.H. Chen, E.R. Hawkes, Proc. Combust. Inst. 32 (2009) 1465–1472.
[6] C.S. Yoo, T.F. Lu, J.H. Chen, C.K. Law, Combust. Flame 158 (2011) 1727–1741.
[7] G. Bansal, H.G. Im, Combust. Flame 158 (2011) 2105–2112.
[8] H. Tennekes, J.L. Lumley, A First Course in Turbulence, MIT Press, Cambridge, Mass, 1972.
[9] J.O. Hinze, Turbulence, second ed., McGraw-Hill, New York, 1975.
[10] N. Chakraborty, H. Hesse, E. Mastorakos, Flow Turbul. Combust. 84 (2010) 125–166.
[11] N. Chakraborty, E. Mastorakos, Flow Turbul. Combust. 80 (2008) 155–186.
[12] K.W. Jenkins, M. Klein, N. Chakraborty, R.S. Cant, Combust. Flame 145 (2006) 415–434.
[13] D. Thevenin, Proc. Combust. Inst. 30 (2005) 629–637.
[14] D. Thevenin, O. Gicquel, J. De Charentenay, R. Hilbert, D. Veynante, Proc. Combust. Inst. 29 (2002) 2031–2039.
[15] M. Day, T. Shigeru, B. John, L. Michael, B. Vince, Robert K C. Combust. Flame 159 (2012) 15.
[16] J.H. Chen, Proc. Combust. Inst. 33 (2011) 99–123.
[17] S. Sreedhara, K.N. Lakshmisha, Proc. Combust. Inst. 29 (2002) 2051–2059.
[18] C.D. Pierce, Progress-variable approach for large-eddy simulation of turbulent combustion, Ph.D. Thesis, Stanford University, 2001.
[19] J.B. Bell, M.S. Day, C.A. Rendleman, S.E. Woosley, M.A. Zingale, J. Comput. Phys. 195 (2004) 677–694.
[20] M.S. Day, J.B. Bell, Combust. Theor. Model 4 (2000) 535–556.
[21] H.N. Najm, P.S. Wyckoff, O.M. Knio, J. Comput. Phys. 143 (1998) 381–402.
[22] O.M. Knio, H.N. Najm, P.S. Wyckoff, J. Comput. Phys. 154 (1999) 428–467.
[23] G. Strang, SIAM J. Numer. Anal. 5 (1968) 11.
[24] G.S. Jiang, C.W. Shu, J. Comput. Phys. 126 (1996) 202–228.
[25] R. Yu, J.F. Yu, X.S. Bai, J. Comput. Phys. 231 (2012) 5504–5521.
[26] P.N. Brown, G.D. Byrne, A.C. Hindmarsh, SIAM J. Sci. Stat. Comput. 10 (1989) 1038–1051.
[27] J. Li, Z.W. Zhao, A. Kazakov, F.L. Dryer, Int. J. Chem. Kinet. 36 (2004) 566–575.
[28] H.N. Najm, O.M. Knio, J. Sci. Comput. 25 (2005) 263–287.
[29] R.H. Kraichna, Phys. Fluids 13 (1970) 22.
[30] J. Jeong, F. Hussain, J. Fluid Mech. 285 (1995) 69–94.
[31] R. Yu, X.S. Bai. Int. J. Numer. Methods Fluids (2012).
[32] P. Sagaut, C. Cambon, Homogeneous Turbulence Dynamics, Cambridge University Press, Cambridge, New York, 2008.
[33] J. Bell, M. Dayl, A. Almgren, M. Lijewski, C. Rendleman, R. Cheng, I. Shepherd, J. Phys. Conf. Ser. 46 (2006) 1–15.
[34] N. Chakraborty, G. Hartung, M. Katragadda, C.F. Kaminski, Combust. Flame 158 (2011) 1372–1390.
[35] S.B. Pope, P.K. Yeung, S.S. Girimaji, Phys. Fluids A – Fluid 1 (1989) 2010–2018.